

Near, far, wherever you are: simulations on the dose efficiency of holographic and ptychographic coherent imaging

Ming Du¹, Dogă Gürsoy^{2,3}, and Chris Jacobsen^{2,4,5,*}

¹Department of Materials Science, Northwestern University, Evanston, IL 60208, USA

²Advanced Photon Source, Argonne National Laboratory, Argonne, IL 60439, USA

³Department of Electrical Engineering and Computer Science, Northwestern University, Evanston, IL 60208, USA

⁴Department of Physics and Astronomy, Northwestern University, Evanston, IL 60208, USA

⁵Chemistry of Life Processes Institute, Northwestern University, Evanston, IL 60208, USA

*To whom correspondence should be addressed; E-mail: cjacobsen@anl.gov

Abstract

Different studies in x-ray microscopy have arrived at conflicting conclusions about the dose efficiency of imaging modes involving the recording of intensity distributions in the near (Fresnel regime) or far (Fraunhofer regime) field downstream of a specimen. We present here a numerical study on the dose efficiency of near-field holography versus ptychography, a variant of far-field coherent diffraction imaging (CDI) involving multiple overlapping finite illumination positions. Unlike what has been reported for single-illumination CDI, we find that the quality, measured by spatial resolution and mean error, of reconstructed images from ptychography is similar (though slightly better) to what one can obtain from near-field holography at identical fluence on the specimen. These results support the concept that, if the experiment and image reconstruction are done properly, the sample can be near, or far; wherever you are, photon fluence on the specimen sets one limit to spatial resolution.

1 Introduction

X-ray microscopy provides a unique combination of short wavelength radiation (with the potential for nanoscale imaging), with high penetration. However, X rays ionize atoms, so radiation damage often sets a limit on the achievable resolution, especially when studying soft or biological materials [1, 2]. This becomes quite important as one seeks finer spatial resolution δ_r , since for isotropic objects there is a tendency [3, 4] for the required number of photons per area incident on the specimen (the fluence n_{ph}) to obtain an image with sufficient signal-to-noise ratio to increase as $n_{\text{ph}} \propto (\delta_r)^{-4}$. Since fluence leads directly to the absorbed radiation dose D , it is important to use low-fluence methods for high resolution imaging.

One of the methods for low-fluence and low-dose x-ray imaging is to use phase contrast. That is because [5, 6] the phase shift imparted on an x-ray wavefront scales like $\rho Z \lambda^2$, while beam absorption scales like $\rho Z \lambda^4$, where ρ is the density, Z is the atomic number, and λ is the wavelength. As a result, phase contrast often leads to reduced radiation dose for the same feature detectability, especially at shorter wavelengths [7].

While the phase of an x-ray wave cannot be measured directly, it can be inferred by mixing with a reference wave so that phase changes are encoded as intensity differences. This can be done using the Zernike method with x-ray zone plates [8], or by using beam propagation. Over short propagation distances, one or a few Fresnel fringes can be interpreted using approaches such as the transport of intensity [9], while at intermediate distances a large number of Fresnel fringes allow for in-line holographic reconstruction [10, 11]. If the beam is allowed to propagate to a distance that meets the far-field or Fraunhofer condition, x-ray images of phase objects can be recovered from coherent diffraction patterns with no wave mixing required [12]. This can be done in a single illumination approach now called coherent diffraction imaging or CDI [13] where one uses finite support iterative phase retrieval [14]. Alternatively, it can be done using multiple finite-sized overlapping coherent illumination spots in a method called ptychography [15, 16], where one

again uses an iterative phase retrieval algorithm [17] to obtain an image with a spatial resolution much finer than the size of the illumination spot [18].

Are there fundamental differences in photon exposure requirements depending on whether one mixes the specimen wave with a reference to get intensities, or measures the specimen wave diffraction intensities alone? One might think that by mixing a strong reference wave R with a weak specimen wave S one might have a multiplying effect due to the net intensity recording being $|R|^2 + RS^\dagger + R^\dagger S + |S|^2$, and indeed it has been claimed that near-field x-ray holography is especially dose-efficient [19, 20]. However, the quantum noise is still limited by the specimen wave, leading to the following conclusion by Richard Henderson [21] in the context of electron microscopy: “It can be shown that the intensity of a sharp diffraction spot containing a certain number N of diffracted quanta will be measured with the same accuracy (\sqrt{N}) as would the amplitude (squared) of the corresponding Fourier component in the bright field phase contrast image that would result from interference of this scattered beam with the unscattered beam [22]. The diffraction pattern, if recorded at high enough spatial resolution, would therefore contain all the intensity information on Fourier components present in the image.” That is, the reconstruction of a certain spatial frequency of the object should be equally accurate for far-field diffraction, and for near-field phase contrast imaging, provided both use the same fluence n_{ph} on the specimen.

One could argue that the act of recovering phases from far-field diffraction patterns can introduce extra noise. Indeed, Henderson followed the comments above [21] with this statement: “It [the diffraction pattern] would lack only the information concerning the phases of the Fourier components of the image which are of course lost. Thus, for the same exposure, holography should be equal to normal phase contrast in performance, and diffraction methods inferior because of the loss of the information on the phases of the Fourier components of the image.” However, diffraction patterns *are* affected by the phase of Fourier components. Consider the example of a transverse shift of one subregion of a coherently illuminated object: the shift theorem of the Fourier transform makes it clear that one would change the phase of that subregion’s contribution to a specific point in the entire object’s complex diffraction amplitude. Therefore the intensity of the diffraction pattern produced by the object would undergo some redistribution (that is, the speckle pattern would change), showing that diffraction methods do indeed involve the encoding of phase. This is perhaps why a number of studies on iterative phase retrieval methods have indicated that the phase retrieval process seems not to add additional noise to the reconstructed image beyond that present in the diffraction pattern itself [14, 23, 24, 25, 26].

We would therefore conclude that the fluence n_{ph} on the object limits resolution, rather than the use of near-field versus far-field imaging methods. However, conventional CDI is particularly challenging as a far-field imaging method. The reconstruction of complex objects from their single coherent diffraction patterns is not always straightforward, as one needs precise knowledge of the specimen’s support S (the subregion within which the object is restricted to lie [27, 28]). In addition, other experimental limitations like the loss of a significant subset of strong, low-spatial-frequency intensity values can complicate object reconstruction [29, 28]. These complications may have played a role in a simulation study that showed that near-field holography yields superior images at the same fluence n_{ph} when compared to standard CDI as a far-field imaging method [20].

The problems noted above for standard CDI are greatly mitigated in ptychography, where the finite coherent illumination spot provides several benefits. Ptychography allows one to accurately determine a finite support not due to the characteristics of the object, but instead due to the characteristics of the probe function, which is recovered from the data. Object subregions that are present in the overlap between two probe positions provide a sort of holographic reference between the two resulting diffraction patterns [30]. Finally, the spreading of the unmodulated probe function in the far field (due to its finite extent at the object’s plane) helps distribute intensities out of the central, zero-spatial-frequency pixel on the diffraction detector, especially when the probe is a convergent beam provided by the focus of a lens [31]. Therefore while standard CDI often shows imperfections in image reconstruction beyond those provided by fluence, one has hope that ptychography can provide a method for a more robust comparison between the fluence requirements of near-field versus far-field coherent imaging methods. It is for these reasons that we have carried out a simulation study comparing near-field holography against ptychography as a far-field imaging method.

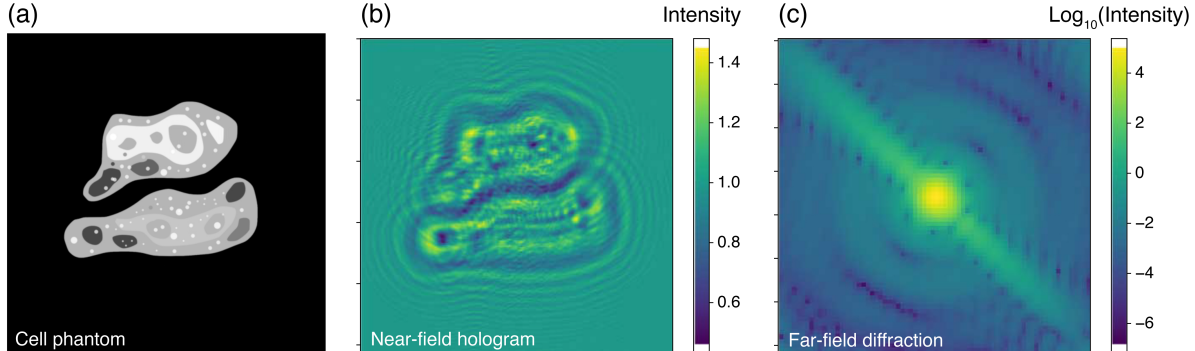


Figure 1: The 512×512 pixel phantom cell object used for our computational experiments (a), along with the simulated experimental intensities for near-field holography with propagation by a distance corresponding to a per-pixel Fresnel number (Eq. 3) of 10^{-3} (b), and standard far-field coherent diffraction imaging (CDI) for the entire object illuminated at once (c) shown here on a logarithmic intensity scale. In fact, a set of far-field diffraction intensity patterns were simulated for a series k of different illumination or probe positions across the sample, which is the type of dataset one obtains in ptychography. The object is the same pure-phase cell phantom used in a prior study [20], so that one can compare directly with those results. The only difference is that we used the complex conjugate of the phantom so as to have positive rather than negative phase shifts, since x-ray phase is advanced rather than retarded in materials [38].

2 Image reconstruction method

In order to compare near-field holography against ptychography, we have chosen to use the same optimization-based reconstruction method for the two imaging approaches as will be described below, so as reveal only the inherent differences between them. The work of Hagemann and Salditt [20] used the relaxed averaged alternating reflections or RAAR algorithm [32] for reconstruction. While we have chosen to make use of the same simulated object that they used (Fig. 2(a) of [20]), in our case, we have chosen to use a more basic cost function minimization approach, in which one defines a forward model for how incident illumination interacts with a present guess of the specimen to produce a measurable intensity distribution, after which one seeks adjust the guess so as to minimize the difference between the result of this forward model and the actual measured intensity distribution (we refer to this difference as the cost function C). One can also include regularizers in this approach as will be described below. In order to efficiently minimize the cost function C for the two different imaging methods of near-field holography and far-field ptychography, we have chosen to use an automatic differentiation (AD) approach [33] so that we do not need to calculate gradients of C by hand for the two imaging methods and regularizers. The use of AD in coherent diffraction imaging was suggested before powerful parallelized toolkits were widely available [34], but it has since been used for image reconstruction in ptychography [35], in Bragg and near-field ptychography [36], and in near-field holography of thick specimens [37].

Our approach is to minimize the cost function C by adjusting the object function \mathbf{n} which contains the complex refractive index of the sample. For x-ray imaging, we used a 2D grid of the x-ray refractive index $n(x, y) = 1 - \delta(x, y) - i\beta(x, y)$ distribution multiplied by the projection object thickness $t(x, y)$ to yield an optical modulation of $\exp\{k[i\delta(x, y) - \beta(x, y)]t(x, y)\}$ in the sign convention where forward propagation is $\exp[-ikz]$. In our case, we used the same 512×512 pixel pure-phase cell phantom (shown here in Fig. 1(a)) as was used in prior work [20], with the modification of taking its complex conjugate so that it had positive rather than negative phase values since x-ray phase is advanced rather than retarded in materials [38]. Within the 19.4% of the pixels that define the support S of the object, it produces an optical modulation \mathbf{n}_0 on the incident illumination with a mean phase of

$$\bar{\varphi} = 0.643 \text{ radians}, \quad (1)$$

a variance of $\sigma_\varphi = 0.037$ radians, and a bound of 0 to 1 radians (this object phase contrast is representative of what one might have in soft x-ray imaging; the contrast is usually lower in hard x-ray imaging). The

cost function C is the mean squared difference between the modulus of the wave at the detector plane as predicted by the forward model $f(\mathbf{n}, k, d)$ for the present guess \mathbf{n} of the object, and the “measured” intensity y_k of

$$y_k = |f(\mathbf{n}_0, k, d)|^2, \quad (2)$$

where d is the free-space propagation distance z in terms of a Fresnel number

$$d = \frac{\Delta^2}{\lambda z} \quad (3)$$

for an object pixel size Δ (so that far-field diffraction has $d = 0$). Fresnel propagation $f(\mathbf{n}, k, d)$ of the wavefield leaving the specimen to the detector plane was accomplished via convolution with a propagator function in the Fourier domain [39]. Poisson noise was incorporated in recorded intensity values y_k as will be described below. We then had a least-square or LSQ cost function C_{LSQ} between the intensities one would expect from the present guess of the object, versus the measured intensities y_k , of

$$C_{\text{LSQ}} = \frac{1}{N_p N_k} \| |f(\mathbf{n}, k, d)| - \sqrt{y_k} \|_2^2. \quad (4)$$

where N_p represents the number of pixels in the detector, and N_k represents the number of illumination spots k ($N_k = 1$ for the single, full-area illumination in holography).

The formulation of the cost function in Eq. 4 is straightforward: by minimizing the cost function, we update the object function \mathbf{n} so that the Euclidean distance between the diffraction images generated by \mathbf{n} and the actual measurements is reduced. A least square (LSQ) cost function like this is more appropriate for images containing Gaussian noise which is generally available with relatively high photon fluences [40], but is unable to accurately account for the shot noise at low photon fluences. When the object is illuminated by a limited number of photons, the total probability of observing the entire set of experimental measurement given the object function \mathbf{n} is better described by a Poisson distribution as

$$p(\mathbf{y}|\mathbf{n}) = \prod_{i=1}^{N_p N_k} \frac{e^{-|f(\mathbf{n}, k, d)|_i^2} |f(\mathbf{n}, k, d)|_i^{2y_i}}{y_i!}. \quad (5)$$

Eq. 5 is also known as the Poisson likelihood function, and the true object function should be one that maximizes the likelihood. In practice, the negative logarithm of Eq. 5 is often taken, so that the maximization of a serial product can be turned into the more tractable problem of minimizing a sum. In this way, the Poisson cost function is written as

$$C_{\text{Poisson}} = \frac{1}{N_p N_k} \sum_{i=1}^{N_p N_k} (|f(\mathbf{n}, k, d)|_i^2 - 2y_i \log |f(\mathbf{n}, k, d)|_i). \quad (6)$$

In ptychography, the lack of scattering that takes place when the illuminating probe function is outside the object’s boundary means that it is quite natural for a reconstruction algorithm to seek solutions for such regions that are empty, even under conditions of limited illumination. To add a similar constraint to near-field hologram reconstructions, we added to the cost function of Eq. 4 a regularizer consisting of a finite support mask S . This yields an update \mathbf{n}' to the object of

$$\begin{aligned} \mathbf{n}' &= \underset{\mathbf{n}}{\text{arg min}}(C_j) \\ &\text{subject to } n_w = 0 \text{ for } n_w \notin S \text{ and } n \geq 0 \text{ for } n \in S \\ &\text{where } m \in \{\text{LSQ, Poisson}\} \end{aligned} \quad (7)$$

so that both ptychography and holography should seek solutions that minimize fluctuations in regions outside the support. A finite support constraint also suppresses the twin-image in in-line holography [41].

With the forward model as described above, and the finite support constraint added to near-field holography, we were able to obtain reconstructed images by minimization of the cost function C , using either the LSQ or the Poisson cost function. The partial derivative of C with regards to the elements of \mathbf{n} was calculated using automatic differentiation (AD) as implemented as a cost function in TensorFlow [42], so that both experiments (holography and ptychography) and both cost function types (LSQ and Poisson) could be treated in the same way simply by varying the Fresnel number d . The ADAM optimizer [43] in TensorFlow was used to update the object function using the calculated gradients.

3 Numerical experiments

For direct comparison with prior work [20], we used the same 512×512 pixel simulated cell phantom phase object described above, and the same value of the Fresnel number (Eq. 3) of $d = 10^{-3}$ for near-field holography. This corresponds to $z = 40.3 \mu\text{m}$ with $\Delta = 10 \text{ nm}$ pixel size at a soft x-ray photon energy of 500 eV, or $z = 807 \mu\text{m}$ at a hard x-ray photon energy of 10 keV. In the case of holography, the object was padded by 256 pixels on each side before optical propagation is carried out in order to prevent fringe wraparound due to the periodic array nature of discrete Fourier transforms. For ptychography, we assumed a probe function that was Gaussian in both magnitude and phase, with a standard deviation of 6 pixels and a phase that varied from 0 to 0.5 radians. The shift between probe positions was set to 15 pixels so that there was good probe overlap at high fluence as is required for robust ptychographic reconstructions [30]. This led to a square scan grid with 33×34 probe positions, and for each probe position a 72×72 pixel subset of the object array was extracted before multiplication with the probe function and calculation of the resulting 72×72 pixel diffraction pattern.

X-ray microscopes use ionizing radiation, so it is important with many specimen types to limit the photon fluence n_{ph} (incident photons per pixel) and consequent radiation dose that the specimen receives. However, must supply sufficient fluence in order to successfully image small, low contrast features. For phase contrast imaging of a non-absorbing, low-contrast specimen with thickness t_f and phase-shifting part of the refractive index δ_f for feature-containing pixels and δ_b for background (feature-free) pixels, one can estimate that the fluence required to obtain an image with a signal to noise ratio of SNR is given by Eq. 39 of [6], which we rewrite here as

$$n_{\text{ph}} = \frac{\text{SNR}^2}{2} \frac{1}{k^2 |\delta_f - \delta_b|^2 t_f^2} \quad (8)$$

where $k \equiv 2\pi/\lambda$ is the wavenumber. Since $k|\delta_f - \delta_b|t_f$ is the mean phase shift within the object compared to the object-free region, we can substitute this with $\bar{\varphi} = 0.643$ radians from Eq. 1 and obtain an estimate that we require a fluence of

$$n_{\text{ph}} = \text{SNR}^2 / [2(\bar{\varphi})^2]. \quad (9)$$

Given that the variance about the mean phase within the object was $\sigma_\varphi = 0.037$ radians, we would expect that a signal to noise ratio of about $|\bar{\varphi}|/\sigma_\varphi = 17.4$ would begin to give very faithful, low noise representations of the true object, which corresponds to a fluence estimate of $n_{\text{ph}} = 350$ photons per pixel (and with higher fluences giving increasing image fidelity).

We therefore carried out simulations with values of n_{ph} that bracketed a value of $n_{\text{ph}} = 350/\text{pixel}$ on an approximately logarithmic scale. Starting from the noise-free “recorded” intensities y_k of Eq. 2 for both the single large hologram intensity and for the set of ptychographic diffraction intensity patterns, we incorporated Poisson noise to y_k for a specified total fluence n_{ph} in photons per pixel on the specimen. Because we expect $n_{\text{ph}} = 350/\text{pixel}$ to be the nominal dividing line between “high-dose” and “low-dose” regimes, datasets with n_{ph} beyond that were reconstructed using the LSQ cost function which approximates photon noise using a quasi-Gaussian model that works well at high photon fluence. On the other hand, data with n_{ph} below $350/\text{pixel}$ were reconstructed using both the LSQ and the Poisson cost function. Two separate, independent random noise datasets were generated for each experiment type, fluence, and loss function type; reconstructed images from one of these two instances are shown in Fig. 2. This figure shows that both near-field holography and ptychography yield high quality reconstructions at high photon fluence. As the fluence decreases to $n_{\text{ph}} = 350/\text{pixel}$ incident photons per pixel or less, the images begin to show a degradation in quality, but in different ways. In near-field holography, the images begin to take on a “salt and pepper” or speckle-like noise appearance as one would expect in a direct coherent imaging experiment. Switching to the Poisson cost function does not help significantly with improving the quality. In ptychography at low fluence, one will have relatively few photons scattered outside the numerical aperture of the probe function, so the image appears to show a loss of spatial resolution going towards the probe resolution but with less “salt and pepper” noise appearance. At very low fluences in ptychography, there are relatively few photons in the overlap regions between probe positions, so one starts to see the scan grid artifacts that can arise due to insufficient probe overlap when using the LSQ cost function [30, 44]. The Poisson cost function, however, is able to effectively suppress the grid artifacts, and gives sharper boundaries of features compared to the LSQ cost function, especially for n_{ph} below $35/\text{pixel}$. Nevertheless, results of the Poisson

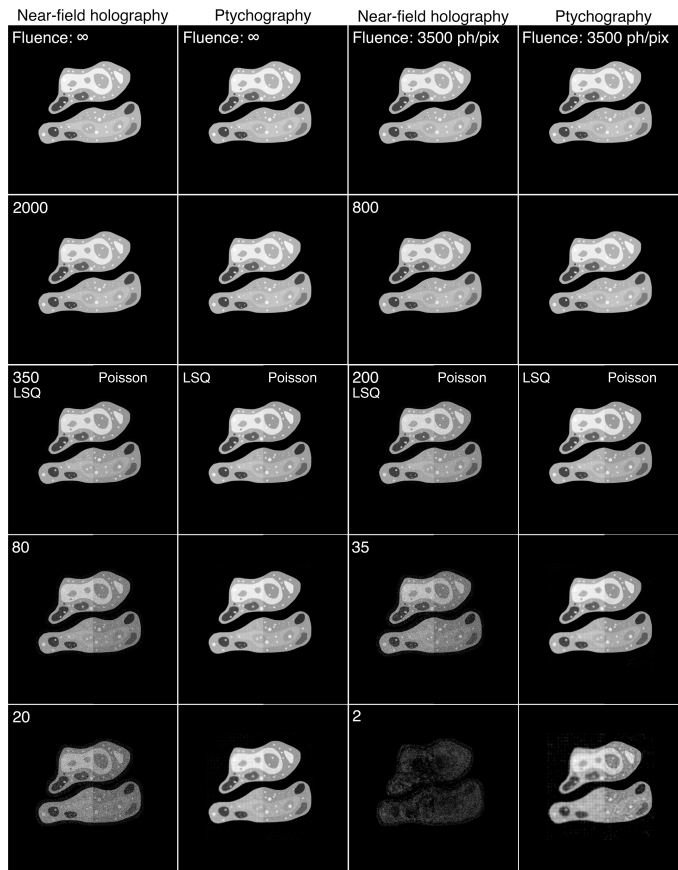


Figure 2: Reconstructed images of the cell phantom shown in Fig. 1(a) obtained for both near-field holography, and ptychography, at the photon fluences n_{ph} indicated. For a photon fluence higher than 350 photons per pixel, only results obtained using the least square (LSQ) cost function are shown; for fluences on or below that, we show the reconstructions yielded by both the LSQ cost function (Eq. 4) and the Poisson cost function (Eq. 6), which are placed side-by-side. At high photon fluence, both holography and ptychography yield high quality images. However, their behaviors differ at low fluence. For holography, the images gain a more salt-and-pepper appearance as one would expect from low photon statistics. The use of the Poisson noise model does not significantly improve the reconstruction quality. In ptychography, the decrease in photons scattered beyond the illumination probe’s numerical aperture at low fluence means the images tend more and more towards the probe’s limit towards spatial resolution; in addition, at very low fluence there are few photons in the “tails” of the probe function so one begins to see a scan grid artifact associated with insufficient probe overlap when the image is reconstructed using the LSQ cost function [30, 44]. On the other hand, the grid artifact is effectively suppressed in the results of the Poisson cost function, and the features retain more of their sharpness, though sometimes one also sees fringe-like artifacts such as what is highlighted in the yellow box at a fluence of 35/pixel.

cost function at relatively high photon fluences incorporate fringe-like artifacts, such as in the region marked by the yellow dashed box in the image with $n_{\text{ph}} = 35/\text{pixel}$. Even when reconstructing noise-free data, this kind of artifact still exists, which proves that the Poisson cost function is not always a superior choice than LSQ and Gaussian cost functions. Another observation adding to this conclusion is that the Poisson cost function generally takes more iterations to converge, especially in the case of ptychography.

In order to better quantify the reconstruction quality, we now consider metrics one can obtain from noisy images. If one has two images I_1 and I_2 of the same object with two different instances of noise, one can calculate an overall image correlation coefficient r of [45]

$$r = \frac{\langle (I_1 - \langle I_1 \rangle) (I_2 - \langle I_2 \rangle)^\dagger \rangle}{\sqrt{\langle (I_1 - \langle I_1 \rangle)^2 \rangle \langle (I_2 - \langle I_2 \rangle)^2 \rangle}}. \quad (10)$$

One can then use this correlation coefficient to calculate an overall image signal-to-noise ratio [46] or SNR of

$$\text{SNR} = \sqrt{\frac{r}{1-r}} \quad (11)$$

where the expression of Eq. 11 is correct for intensity images I_1 and I_2 , as confirmed by the as-expected scaling of $\text{SNR} \propto \sqrt{n_{\text{ph}}}$ [47]. The result of using this measure within the finite support regions is shown in Fig. 3(a). The least-square-fit slopes for near-field holography and ptychography reconstructed using LSQ are both near 0.5 as expected for $\text{SNR} \propto \sqrt{n_{\text{ph}}}$, though the ptychography reconstructions show a higher SNR. At low fluences especially, this higher SNR may be due in part to a correlation of low-probe-overlap scan grid artifacts along with the correlation of image features; this may also explain why the slope is slightly below 0.5 for ptychography. As one compares the results yielded by the two types of cost functions, it can be found that while the SNR of near-field holography is slightly enhanced at $n_{\text{ph}} = 0.8$ and $2/\text{pixel}$, the SNR of ptychography reconstructions with Poisson cost function is actually lower than those with LSQ, and the disparity increases at higher n_{ph} . This observation seems to contradict the visual appearance of images in Fig. 2, where Poisson reconstructions give sharper feature boundaries under low dose conditions; however, it is in fact reasonable because the artifacts in Poisson reconstructions are more uncorrelated compared to the dot-grids and blurriness of LSQ reconstructions. In Poisson reconstructions, the fringe artifacts are heavily dependent on the initial guess. As the initial guess was created by Gaussian noise, the positions and amounts of the fringes can vary even for two reconstructions corresponding to the same n_{ph} . As a result, the SNR metric of Eq. 11 tends to interpret the artifacts in ptychography reconstructions with Poisson cost function as uncorrelated noise.

Since the phantom cell is a pure phase object with a well-defined support S (which was used in the near-field holography reconstruction to suppress the twin image), another whole-image metric we can use is the within-support mean squared error (SMSE) on the phase of

$$\text{SMSE} = \frac{1}{\sum_{n \in S} 1} \sum_{n \in S} \|\arg(\text{phantom}) - \arg(\text{reconstruction})\|^2 \quad (12)$$

where n is a pixel index. This is the same ℓ_2 -norm metric defined by Eq. 9 in prior work [20], where it was found that near-field holography gave a higher SMSE at fluences below about 100 quanta per pixel when compared to far-field CDI, but that holography then gave a lower SMSE at higher fluences. Our results for the SMSE for near-field holography and ptychography are shown in Fig. 3(b), which shows virtually the same trend and relation as in Fig. 3(a): first, ptychography provides results with lower error compared to holography; and second, use of the Poisson cost function (Eq. 6) gives slightly better results than LSQ (Eq. 4) for holography, but appears to result in larger SMSE for ptychography, again due to the more uncorrelated artifacts in Poisson reconstructions.

Although whole-image SNR and SMSE measurements show that ptychography slightly outperforms near-field holography at low photon fluence, they also seem to indicate improved results for ptychography when using the LSQ cost function (Eq. 4) instead of the Poisson cost function (Eq. 6) which seems to contradict the visual appearance of the reconstructed images shown in Fig. 2. We therefore compared the performance of the two ptychography reconstructions for reconstructing a small, bright feature indicated by a yellow arrow in Fig. 4. For each reconstructed image, a Gaussian fit was carried out on this feature with a 2D

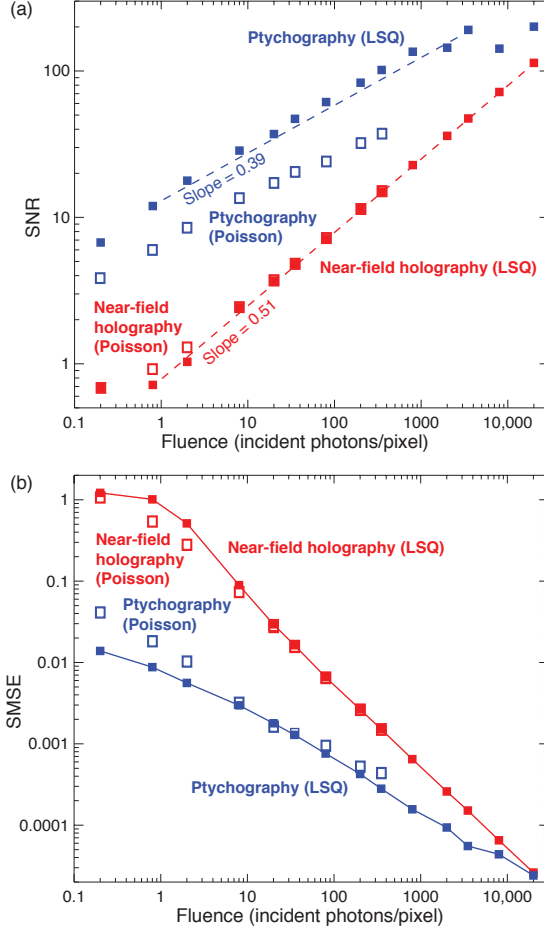


Figure 3: Whole image metrics of image reconstructed image quality as a function of fluence n_{ph} . At top (a) is shown the signal-to-noise ratio (SNR) as calculated using Eq. 11 for near-field holography and for ptychography. The image correlation was calculated within the finite support area of the object, since this was used as an enforced constraint in near-field holography (Eq. 8) while in ptychography the lack of object scattering when the probe is illuminating areas outside the support constraint produces a similar effect. At each photon fluence n_{ph} and for each cost function type, two separate instances of Poisson noise were generated. The slope for both least square (LSQ) error curves is near 0.5, indicating that the SNR increases roughly as $\sqrt{n_{\text{ph}}}$, as one might expect. In ptychography, the SNR at lower exposure levels might be artificially high due to the low-fluence scan grid artifact noted in Fig. 2, which is a correlated artifact adding to correlated image information. At bottom (b) is shown the within-support mean squared error (SMSE) of Eq. 12, which again shows improved performance at low fluences for ptychography compared to near-field holography. However, both plots show slightly worse performance of the Poisson cost function (Eq. 6) compared to LSQ (Eq. 4) even at low n_{ph} .

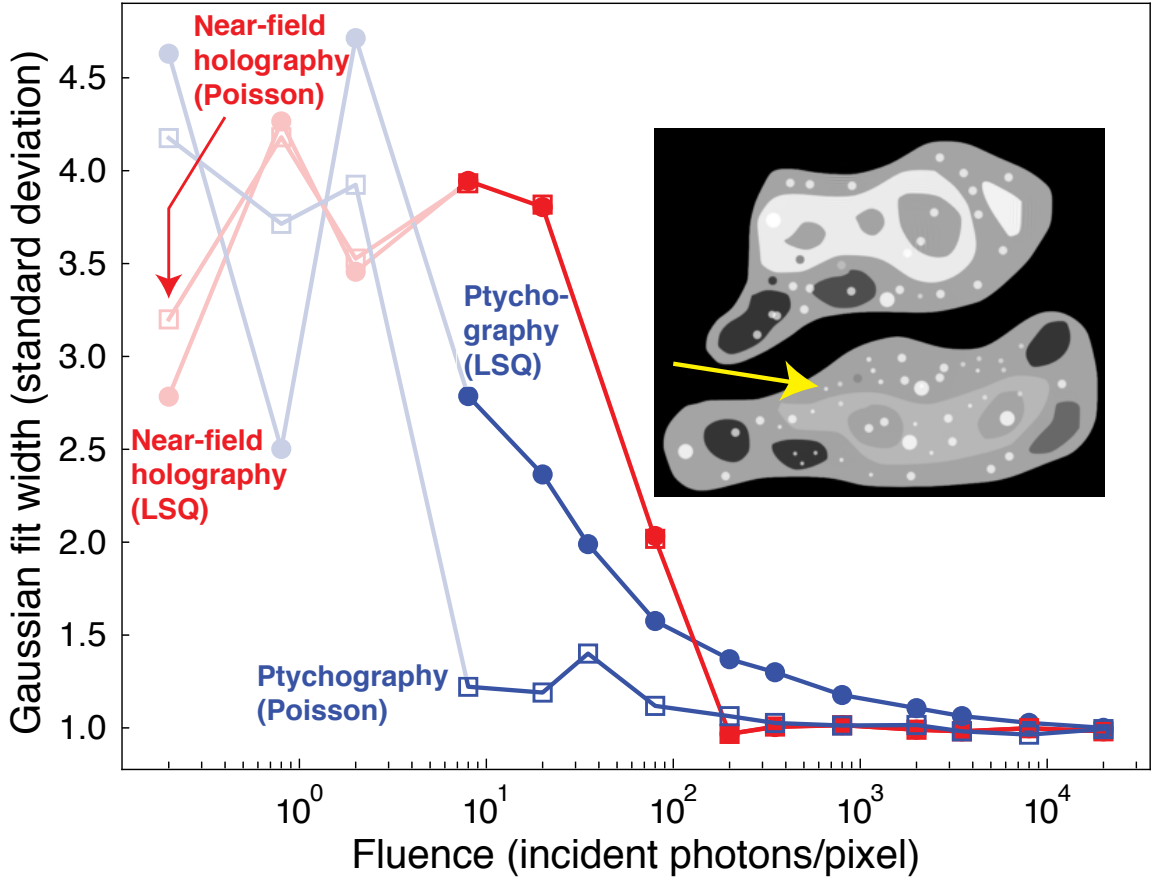


Figure 4: Standard deviation of the fitted Gaussian 2D profile for the small bright-spot-like feature pointed to by the yellow arrow. For photon fluences below 2/pixel, the curves are greatly influenced by uncertainties, but meaningful results start to appear at higher photon fluences (with one outlier removed at $n_{\text{ph}} = 35$ for holography). While the results conform with our observation that ptychography generally leads to better resolution under low dose conditions, it also agrees with the visual appearance of the reconstructions shown in Fig. 2, where features appear sharper when using the Poisson cost function at low photon fluence.

symmetric profile, as shown in Fig. 4. An increase in the standard deviation of the Gaussian fitting function thus measures the blurriness of the reconstructed image, since a sharper feature will have a smaller standard deviation. At very low photon fluence, the overall resolution of the images is low, and the fitted standard deviation may suffer from significant uncertainty. With $n_{\text{ph}} > 2/\text{pixel}$, the results start to show less fluctuation (one outlier for holography at $n_{\text{ph}} = 35/\text{pixel}$ has been removed from the plot). For $n_{\text{ph}} < 200/\text{pixel}$, ptychography gives a sharper image of specimen features, which agrees with the previous conclusions drawn from SNR and SMSE analyses. In addition, the Gaussian spread of the feature in Poisson-ptychography is smaller than LSQ-ptychography, which indicates that the former gives a sharper appearance to the feature being investigated. This agrees with visual perception of the results shown in Fig. 2.

Another important metric for evaluating two separate instances of equally noisy images is to examine the correlation of their Fourier transforms as a function of radial spatial frequency u_r , leading to the Fourier shell correlation for 3D images or the Fourier ring correlation (FRC) for 2D images [48, 49] given by

$$\text{FRC}_{12}(u_{r,i}) = \frac{\sum_{u_r \in u_{r,i}} F_1(r) \cdot F_2(r)^\dagger}{\sqrt{\sum_{u_r \in u_{r,i}} F_1^2(r) \cdot \sum_{u_r \in u_{r,i}} F_2^2(r)}}. \quad (13)$$

High resolution, low noise images will show strong correlation at high spatial frequencies, while lower res-

olution, noisier images will show poorer correlation at high spatial frequencies. It is common to assign a spatial resolution value based on the crossing of the FRC with a half-bit threshold value [50]. The resulting FRC analysis (plotted only for LSQ results) shown in Fig. 5 indicates that both near-field holography and ptychography deliver full-resolution images at high photon fluences, but that ptychography gives slightly superior results. This figure also highlights the half-bit resolution FRC crossing point with a red circle for the case of an incident fluence of 8 quanta per pixel for each imaging method. This measure of the spatial resolution as a fraction of the $1/(2\Delta_r)$ Nyquist spatial frequency is shown in Fig. 6(a), where one can see that both imaging methods approach full resolution at a fluence near the estimate of 350 quanta per pixel found using Eq. 9. Because of the noise fluctuations present in the FRC curves, the FRC/half-bit crossing fraction may show some variations depending on the particular instances of data Poisson noise; this explains the non-smooth trend of the FRC crossing values shown in Fig. 6(a).

Upon comparing the results drawn from the LSQ and Poisson cost functions, one may again observe the seemingly inferior performance of using the Poisson cost function for ptychography, despite the sharper appearance of features in Poisson results perceived visually. This is because the spatial resolution determined in this way measures the spatial frequency at which correlative signals are overwhelmed by uncorrelated noise. Although Poisson ptychography results contain more high-frequency components in their the signal, the FRC-resolution measure is degraded by high-frequency “noise” due to artifacts such as the fringes shown in the yellow box in Fig. 2. It follows that although the use of a Poisson cost function in ptychography indeed provides sharper features, the fringe artifacts coming along the features can cause misinterpretations to the reconstructed objects in realistic cases when one does not have the prior knowledge that the object is stepwise-constant (that is, for general unknown objects, rather than the phantom cell used in this paper). Thus, a Poisson cost function might not always be the best option, even at low dose conditions.

The fraction of the Nyquist limit spatial frequency shown in Fig. 6(a) was calculated by FRC analysis from two separate instances of Poisson noise at each fluence value and each imaging mode. However, a prior study has carried out FRC analysis by comparing a noisy image against the ground-truth image of the noise-free cell phantom [20]. We have therefore calculated this “ground truth” FRC crossing value, as well as tracing the curves shown in Fig. 4(a) of this previous analysis [20] for both near-field holography and for far-field CDI (where the latter involves a single diffraction pattern from illuminating the entire object array, and the use of a finite support in iterative phase retrieval). We therefore show in Fig. 6(b) up to three FRC/half-bit crossing curves for each experiment type: the same curve from Fig. 6(a) for two noise instances, the crossing obtained by comparing one low-fluence image with the ground truth image, and the traced values from Fig. 4(a) of the previous analysis [20]. As can be seen, there is reasonable agreement between our FRC crossing results and those of the previous analysis [20] for the case of near-field holography with a ground-truth reference, even though the previous analysis used a slightly different reconstruction algorithm (the relaxed averaged alternating reflections or RAAR algorithm [32]). In addition, both ptychography and near-field holography show improved performance relative to far-field CDI, which suffers from well-known difficulties [51, 29, 23, 28]. Another point worthwhile noticing is that, when the FRCs are calculated with regards to the ground truth, the relation between results reconstructed using the LSQ and the Poisson cost function become inverted. This indicates that the Poisson results, especially at low dose conditions, correlate better with the true object in Fourier components with higher spatial frequency. This observation matches visual perception of Fig. 2.

While the above analyses and discussions seem to suggest that ptychography delivers slightly better reconstructed images at low photon fluence, it should also be noted that ptychography is not a replacement for other imaging methods when certain factors in experimental practices are considered. Ptychography acquisition is often more time consuming, and relies on the accurate recording or refinement of probe positions. Also, all our ptychography results shown above were reconstructed with a known probe function. In reality, it is often the case that the probe needs to be reconstructed along with the object, and an imperfectly retrieved probe can lead to artifacts, usually in the form of grids.

4 Conclusion

We have used the same automatic-differentiation-based optimization method for image reconstruction to compare the performance of near-field holography and ptychography at low specimen fluence values. Though this

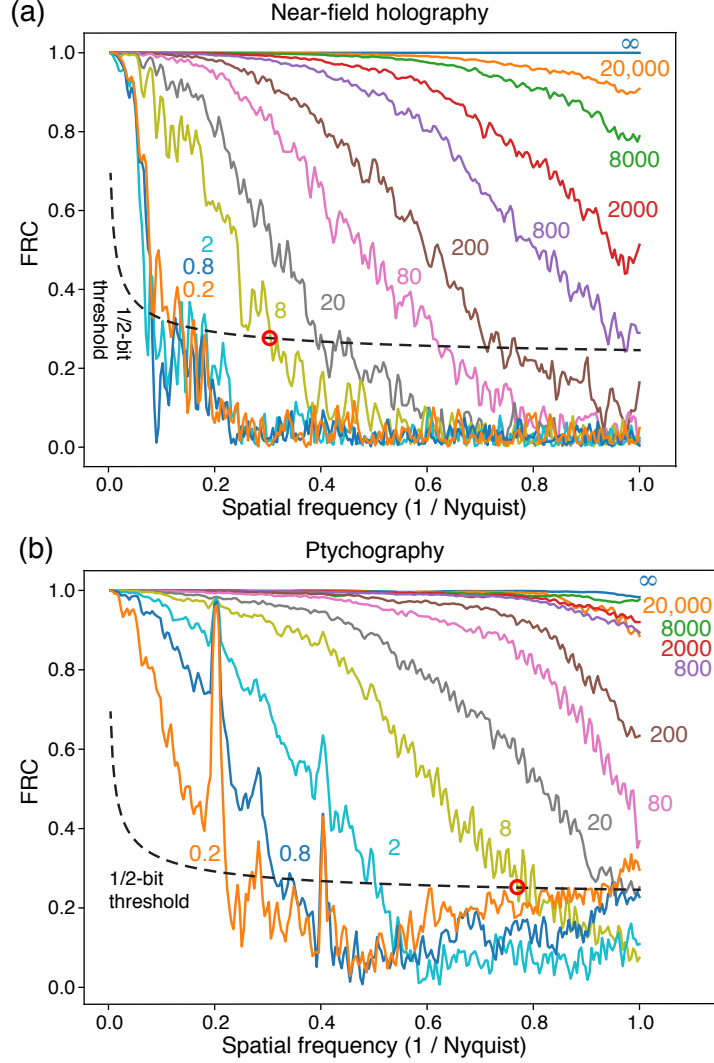


Figure 5: Fourier ring correlation (FRC) curves for two images reconstructed from separate instances of Poisson-noise-included simulated datasets, both for near-field holography (a) and for ptychography (b). Only results obtained using the least square (LSQ) cost function of Eq. 4 are shown. Each curve is labeled with the fluence n_{ph} in quanta per pixel. Also shown on the plot is the 1/2-bit threshold curve that is commonly used to define the achieved spatial resolution based on the spatial frequency of the crossing with the experimental FRC curve [50], as indicated by red circles for a fluence of 8 in both plots. These FRC-crossing normalized spatial frequencies are used in Fig. 6. In near-field holography, the curves shown here exhibit a fairly uniform decline with decreased fluence until one reaches very poor correlation at fluences of 2 or below. In the case of ptychography at low fluence, “spikes” in the FRC curves appearing at a normalized spatial frequency of about 0.2 and harmonics above it are presumably reflective of the strong correlation of the low-fluence scan grid artifact seen in Fig. 2.

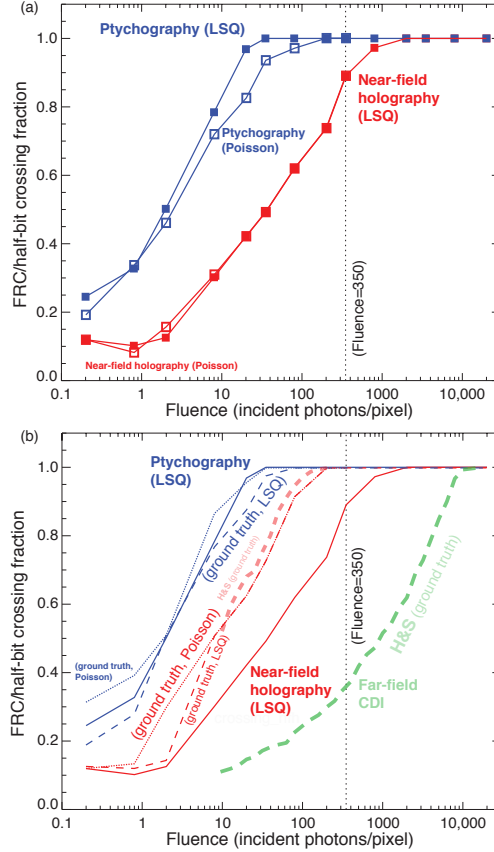


Figure 6: Values for the crossing between the Fourier ring correlation (FRC) curves of Fig. 5 and the half-bit resolution criterion [50], shown as a fraction of the Nyquist spatial frequency limit of $1/(2\Delta_r)$. In (a), this is shown for the FRC analysis between reconstructed images obtained from two instances of Poisson noise, as normally required. The curves are not entirely smooth due to the sensitivity of the FRC crossing on the exact noise instance of the FRC curves shown in Fig. 5, but they show that one achieves full spatial resolution at fluences near the value of 350 quanta per pixel (shown with a vertical dashed line) estimated after Eq. 9. In prior work [20], the FRC crossing analysis was done by comparison of one noise instance with the “(ground truth)” object of the cell phantom, so (b) shows our results for an equivalent “(ground truth)” analysis as dashed lines next to the two-noise-instance analysis results (the same results shown in (a)) as solid lines. Also shown in (b) are the approximate results of the previous study [20] labeled as “H&S (ground truth)” as obtained by tracing of the published figure. (The previous study plotted the FRC crossing as a function of $1/(\Delta_r)$, so we have multiplied the FRC crossing fractions by a factor of 2). As can be seen, our “(ground truth)” results and the “H&S (ground truth)” are reasonably consistent for the case of near-field holography. The previous study also considered far-field CDI, where the entire object array is illuminated and a finite support constraint is applied during iterative reconstruction.

reconstruction algorithm is slightly different than what was used in a previous study [20] that compared near-field holography with single-exposure far-field coherent diffraction imaging (CDI), we have obtained quite similar results for near-field holography as shown in Fig. 6(b), as well as in a comparison of our Fig. 3(b) with Fig. 4(c) of the previous study. The previous study showed that near-field holography gives greatly superior results compared to far-field CDI, but far-field CDI is known to be very challenging due to the experimental difficulty of obtaining an object that has truly zero scattering outside of a defined region (the finite support), and due to the sensitivity of the reconstruction to the correct “tightness” of the support and the accuracy of recording the strong, low-spatial-frequency diffraction signal [51, 29, 23, 28]. Ptychography removes the requirement that the object be limited to being within a finite support constraint, and if a lens focus is used to provide the scanned coherent illumination spot the spreading of the signal in the far-field diffraction pattern helps reduce the dynamic range demands placed on the detector [31]. In addition, the partitioning of data recording into a set of distinct regions of the object may provide some additional information beyond what one obtains when illuminating the entire object in one exposure, which may be why we observe slightly improved performance from ptychography relative to near-field holography in this computational study.

We conclude that the imaging method used does play some role in the quality of an image that one can obtain from a given fluence on the specimen. (We also note that if an optic were to be used to record a direct image with no reconstruction algorithm required, one would need to increase the fluence to account for the focusing efficiency of the optic [24] which is often below 20% for the case of Fresnel zone plates used for x-ray microscopy [52]). However, it is still photon fluence that dominates the achievable reconstruction, as has long been suggested based on theoretical analyses [53, 3, 4, 6]. While previous experiments using near-field holography claimed that one could obtain images at reduced radiation dose compared to far-field imaging methods [19], they did not include a systematic analysis of resolution versus fluence. Such an analysis was included in a prior computational study [20], but it compared near-field holography with far-field CDI rather than with a more robust far-field method like ptychography. We therefore conclude that the sample can be near, or far; wherever you are, photon fluence on the specimen sets a fundamental limit to spatial resolution.

Acknowledgements

This research used resources of the Advanced Photon Source and the Argonne Leadership Computing Facility, which are U.S. Department of Energy (DOE) Office of Science User Facilities operated for the DOE Office of Science by Argonne National Laboratory under Contract No. DE-AC02-06CH11357. We thank the National Institute of Mental Health, National Institutes of Health, for support under grant R01 MH115265. We also thank Celine Dion for inspiration for the title.

References

- [1] Sayre, D., Kirz, J., Feder, R., Kim, D. M. & Spiller, E. Potential operating region for ultrasoft x-ray microscopy of biological specimens. *Science* **196**, 1339–1340 (1977).
- [2] Kirz, J., Jacobsen, C. & Howells, M. Soft x-ray microscopes and their biological applications. *Quarterly Reviews of Biophysics* **28**, 33–130 (1995). Also available as Lawrence Berkeley Laboratory report LBL-36371.
- [3] Sayre, D., Kirz, J., Feder, R., Kim, D. M. & Spiller, E. Transmission microscopy of unmodified biological materials. comparative radiation dosages with electrons and ultrasoft x-ray photons. *Ultramicroscopy* **2**, 337–349 (1977).
- [4] Howells, M. *et al.* An assessment of the resolution limitation due to radiation-damage in x-ray diffraction microscopy. *Journal of Electron Spectroscopy and Related Phenomena* **170**, 4–12 (2009).
- [5] Henke, B. L., Gullikson, E. M. & Davis, J. C. X-ray interactions: Photoabsorption, scattering, transmission, and reflection at $E=50\text{--}30,000$ eV, $Z=1\text{--}92$. *Atomic Data and Nuclear Data Tables* **54**, 181–342 (1993).

- [6] Du, M. & Jacobsen, C. Relative merits and limiting factors for x-ray and electron microscopy of thick, hydrated organic materials. *Ultramicroscopy* **184**, 293–309 (2018).
- [7] Schmahl, G. & Rudolph, D. Proposal for a phase contrast x-ray microscope. In Cheng, P. C. & Jan, G. J. (eds.) *X-ray Microscopy: Instrumentation and Biological Applications*, 231–238 (Springer-Verlag, Berlin, 1987).
- [8] Schmahl, G., Rudolph, D., Schneider, G., Guttman, P. & Niemann, B. Phase contrast x-ray microscopy studies. *Optik* **97**, 181–182 (1994).
- [9] Paganin, D., Mayo, S. C., Gureyev, T. E., Miller, P. R. & Wilkins, S. W. Simultaneous phase and amplitude extraction from a single defocused image of a homogeneous object. *Journal of Microscopy* **206**, 33–40 (2002).
- [10] Baez, A. V. Resolving power in diffraction microscopy with special reference to x-rays. *Nature* **169**, 963–964 (1952).
- [11] Baez, A. V. A study in diffraction microscopy with special reference to x-rays. *Journal of the Optical Society of America* **42**, 756–762 (1952).
- [12] Sayre, D. Prospects for long-wavelength x-ray microscopy and diffraction. In Schlenker, M. *et al.* (eds.) *Imaging Processes and Coherence in Physics*, vol. 112 of *Lecture Notes in Physics*, 229–235 (Springer-Verlag, 1980).
- [13] Miao, J., Charalambous, P., Kirz, J. & Sayre, D. An extension of the methods of x-ray crystallography to allow imaging of micron-size non-crystalline specimens. *Nature* **400**, 342–344 (1999).
- [14] Fienup, J. R. Reconstruction of an object from the modulus of its Fourier transform. *Optics Letters* **3**, 27–29 (1978).
- [15] Hoppe, W. Beugung im Inhomogenen Primärstrahlwellenfeld. I. Prinzip einer Phasenmessung. *Acta Crystallographica A* **25**, 495–501 (1969).
- [16] Hoppe, W. Beugung im inhomogenen Primärstrahlwellenfeld. III. Amplituden- und Phasenbestimmung bei unperiodischen Objekten. *Acta Crystallographica A* **25**, 508–514 (1969).
- [17] Faulkner, H. M. L. & Rodenburg, J. Movable aperture lensless transmission microscopy: A novel phase retrieval algorithm. *Physical Review Letters* **93**, 023903 (2004).
- [18] Rodenburg, J. *et al.* Hard-x-ray lensless imaging of extended objects. *Physical Review Letters* **98**, 034801 (2007).
- [19] Bartels, M., Krenkel, M., Haber, J., Wilke, R. N. & Salditt, T. X-ray holographic imaging of hydrated biological cells in solution. *Physical Review Letters* **114**, 048103 (2015).
- [20] Hagemann, J. & Salditt, T. The fluence–resolution relationship in holographic and coherent diffractive imaging. *Journal of Applied Crystallography* **50**, 531–538 (2017).
- [21] Henderson, R. The potential and limitations of neutrons, electrons and X-rays for atomic resolution microscopy of unstained biological molecules. *Quarterly Reviews of Biophysics* **28**, 171–193 (1995).
- [22] Henderson, R. Image contrast in high-resolution electron microscopy of biological macromolecules: TMV in ice. *Ultramicroscopy* **46**, 1–18 (1992).
- [23] Williams, G., Pfeifer, M., Vartanyants, I. & Robinson, I. Effectiveness of iterative algorithms in recovering phase in the presence of noise. *Acta Crystallographica A* **63**, 36–42 (2007).
- [24] Huang, X. *et al.* Signal-to-noise and radiation exposure considerations in conventional and diffraction x-ray microscopy. *Optics Express* **17**, 13541–13553 (2009).

- [25] Schropp, A. & Schroer, C. G. Dose requirements for resolving a given feature in an object by coherent x-ray diffraction imaging. *New Journal of Physics* **12**, 035016 (2010).
- [26] Godard, P., Allain, M., Chamard, V. & Rodenburg, J. M. Noise models for low counting rate coherent diffraction imaging. *Optics Express* **20**, 25914–25934 (2012).
- [27] Fienup, J. Reconstruction of a complex-valued object from the modulus of its Fourier-transform using a support constraint. *Journal of the Optical Society of America A* **4**, 118–123 (1987).
- [28] Huang, X. *et al.* Incorrect support and missing center tolerances of phasing algorithms. *Optics Express* **18**, 26441–26449 (2010).
- [29] Thibault, P., Elser, V., Jacobsen, C., Shapiro, D. & Sayre, D. Reconstruction of a yeast cell from x-ray diffraction data. *Acta Crystallographica A* **62**, 248–261 (2006).
- [30] Bunk, O. *et al.* Influence of the overlap parameter on the convergence of the ptychographical iterative engine. *Ultramicroscopy* **108**, 481–487 (2008).
- [31] Thibault, P. *et al.* High-resolution scanning x-ray diffraction microscopy. *Science* **321**, 379–382 (2008).
- [32] Luke, D. Relaxed averaged alternating reflections for diffraction imaging. *Inverse Problems* **21**, 37–50 (2005).
- [33] Rall, L. B. *Automatic Differentiation: Techniques and Applications*, vol. 120 (Springer Berlin Heidelberg, Berlin, Heidelberg, 1981).
- [34] Jurling, A. S. & Fienup, J. R. Applications of algorithmic differentiation to phase retrieval algorithms. *Journal of the Optical Society of America A* **31**, 1348–12 (2014).
- [35] Nashed, Y. S. G., Peterka, T., Deng, J. & Jacobsen, C. Distributed automatic differentiation for ptychography. *Procedia Computer Science* **108**, 404–414 (2017).
- [36] Kandel, S. *et al.* Using automatic differentiation as a general framework for ptychographic reconstruction. *Optics Express* **0**, 0 (2019).
- [37] Du, M., Nashed, Y. S. G., Kandel, S., Gursoy, D. & Jacobsen, C. Three dimensions, two microscopes, one code: automatic differentiation for x-ray nanotomography beyond the depth of focus limit. *arXiv.org arXiv:1905.10433* (2019). 1905.10433.
- [38] Larsson, A., Siegbahn, M. & Waller, I. Der experimentelle Nachweis der Brechung von Röntgenstrahlen. *Naturwissenschaften* **12**, 1212–1213 (1924).
- [39] Goodman, J. W. *Introduction to Fourier Optics* (W.H. Freeman, New York, 2017), fourth edn.
- [40] Cai, A. *et al.* Optimization-based image reconstruction in computed tomography by alternating direction method with ordered subsets. *Journal of X-Ray Science and Technology* **25**, 429–464 (2017).
- [41] Liu, G. & Scott, P. D. Phase retrieval and twin-image elimination for in-line Fresnel holograms. *Journal of the Optical Society of America A* **4**, 159–165 (1987).
- [42] Abadi, M. *et al.* Tensorflow: Large-scale machine learning on heterogeneous distributed systems. *CoRR cs.DC*, arXiv:1603.04467 (2016).
- [43] Kingma, D. P. & Ba, J. Adam: A method for stochastic optimization. In *3rd International Conference on Learning Representations*, 1–15 (San Diego, 2015). URL <https://arxiv.org/abs/1412.6980>.
- [44] Huang, X. *et al.* Artifact mitigation of ptychography integrated with on-the-fly scanning probe microscopy. *Applied Physics Letters* **111**, 023103 (2017).
- [45] Bershad, N. & Rockmore, A. On estimating signal-to-noise ratio using the sample correlation coefficient. *IEEE Transactions on Information Theory* **20**, 112–113 (1974).

- [46] Frank, J. & Al-Ali, L. Signal-to-noise ratio of electron micrographs obtained by cross correlation. *Nature* **256**, 376–379 (1975).
- [47] Huang, X. *et al.* Signal-to-noise and radiation exposure considerations in conventional and diffraction x-ray microscopy. *Optics Express* **17**, 13541–13553 (2009).
- [48] Saxton, W. O. & Baumeister, W. The correlation averaging of a regularly arranged bacterial cell envelope protein. *Journal of Microscopy* **127**, 127–138 (1982).
- [49] van Heel, M. Similarity measures between images. *Ultramicroscopy* **21**, 95–100 (1987).
- [50] van Heel, M. & Schatz, M. Fourier shell correlation threshold criteria. *Journal of Structural Biology* **151**, 250–262 (2005).
- [51] Miao, J. *et al.* Quantitative image reconstruction of GaN quantum dots from oversampled diffraction intensities alone. *Physical Review Letters* **95**, 085503 (2005).
- [52] Kirz, J. Phase zone plates for X rays and the extreme UV. *Journal of the Optical Society of America* **64**, 301–309 (1974).
- [53] Glaeser, R. M. Radiation damage and biological electron microscopy. In Siegel, B. M. & Beaman, D. R. (eds.) *Physical aspects of electron microscopy and microbeam analysis*, 205–227 (Wiley, New York, 1975).